ACS APPLIED MATERIALS & INTERFACES

Research Article

www.acsami.org

Partial Conversion of Current Collectors into Nickel Copper Oxide Electrode Materials for High-Performance Energy Storage Devices

Liuyang Zhang and Hao Gong*

Department of Material Science and Engineering, National University of Singapore, Singapore 117576, Singapore

Supporting Information

ABSTRACT: A novel substrate sacrifice process is proposed and developed for converting part of a current collector into supercapacitor active materials, which provides a new route in achieving high energy density of supercapacitor device. Part of a copper foam current collector is successfully converted into highly porous nickel copper oxide electrode for light- and high-performance supercapacitors. Remarkably, this strategy circumvents the problem associated with poor contact interface between electrode and current collector. Meanwhile, the overall weight of the supercapacitor could be minimized. The charge transfer kinetics is improved while the advantage of the excellent mechanical properties of metal current collector is not traded off. By virtue of this unique current collector self-involved architecture, the material derived from the current collector manifests large areal capacitance of 3.13 F cm^{-2} at a current density of 1 A g^{-1}. The capacitance can retain 2.97 F cm^{-2} at a much higher density (4 A g^{-1}). Only a small decay of 6.5% appears at 4 A g^{-1} after 1600 cycles. The strategy reported here sheds light on new strategies in making additional use of the metal current collector. Furthermore, asymmetric supercapacitor using both solid-state gel electrolyte and liquid counterpart are obtained and analyzed. The liquid asymmetric supercapacitor can deliver a high energy density up to 0.5 mWh cm^{-2} (53 Wh kg^{-1}) at a power density of 13 mW cm^{-2} (1.4 kW kg^{-1}).

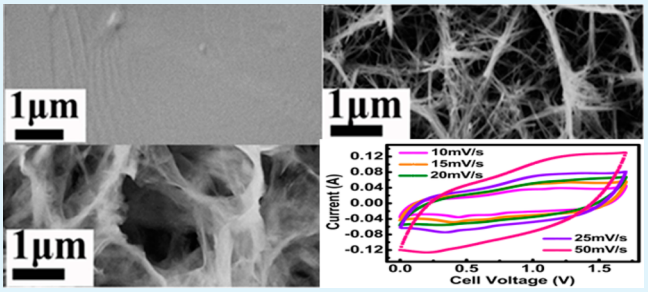

KEYWORDS: *substrate sacrifice, current collector conversion, energy storage, direct growth, nickel copper oxide*

1. INTRODUCTION

The energy crisis places a major strain on existing energy storage devices. There is currently an impending need to delve into efficient and effective energy storage devices such as supercapacitors in addition to batteries. The rapid development of electrochemical capacitors (also known as supercapacitors) has been witnessed in recent years due to their high power density and long cycle life, which allow them to be used in many applications.[1−3] Pseudocapacitive materials based on transitional metal oxides and hydroxides have been demonstrated to be excellent candidates.[4−6] Nickel oxides and several ternary oxides containing nickel such as $NiCo_2O_4$ and $NiMoO_4$ are promising electrode materials by means of their environmentally benign nature, low cost, high theoretical capacitance, and excellent pseudocapacitive properties.[7,8]

Unfortunately, most of the effort has been put only on the active material itself rather than on the entire components of a supercapacitor device as a whole, that is, active materials, current collectors, and electrolytes. When considering the later application and packaging, the match of these three elements needs to be optimized, and an increase in weight percentage of the active material in the whole device is needed. Only then can the overall energy storage capacity be uncompromised.

Hitherto, three fabrication methods have been predominantly used to synthesize electrode materials: (1) slurry-casting a paste containing nanoparticles, binders, and ancillary conducting materials onto a current collector,[9−11] (2) direct growth of electrode nanomaterials on the conductive scaffold/current collector,[12−14] and (3) deposition of a thin-film of active material onto a conductive collector substrate, such as a metal foil or tin-doped indium oxide (ITO)-coated glass.[15] The first method enables electrodes to be made from virtually any powdered material. However, the employment of binder can cause some problems, especially for pseudocapacitive electrodes. For example, some "dead sites" are formed by "burying" the surface of the active material,[16] and this will generate extra contact resistance which deteriorates the performance of the supercapacitor. For the second method, although fast charge/discharge kinetics are observed due to the presence of a highly conductive network throughout the electrode, achieving intimate adhesion between the material and the current collector remains challenging. For the third method, if the thickness of the film is too small, the capacitance and rate capacity may be overestimated. In addition, the total energy storage for such a structure is small. Therefore, it would be beneficial for supercapacitor performance if part of a current collector can be converted into the active electrode material.

Received: April 6, 2015
Accepted: June 22, 2015
Published: June 22, 2015

DOI: 10.1021/acsami.5b02970
ACS Appl. Mater. Interfaces 2015, 7, 15277−15284

Grounded in the aforementioned analysis, we propose and attempt to convert part of a current collector into the electrode material. Though the structure of the current collector (such as nickel foam, copper foam, and stainless steel foam) is three-dimensional (3D) at the macro level, it is still flat at the micro level. Therefore, we attempted to increase the surface area of the foam structure by transfering the flat surface into nanowire structure in situ. The increased surface area/roughness will then facilitate the growth of other active materials on it. We hope that the example this work constitutes could have some application significance. This approach represents a new direction for enhancing the device performance of metal oxide/metal current collector-based electrochemical supercapacitors and can open new opportunities in the near future for designing high-performance energy storage devices.

Herein, the 3D hybrid electrode material was converted from the metal collector via a simple two-step process. First, CuO nanowires were obtained through the controlled oxidation of a piece of copper foam. Next, nickel copper honeycomb-like hybrids were achieved by hydrothermal reaction without the need of hard/soft templates or precipitate-controlling agents. In our proposed approach, the delamination of the electrode from the collector, a problem commonly faced when the electrode is grown on the collector directly, is not observed. This may be because the current collector (Cu) participates in the formation of active electrode in our collector-electrode conversion approach. Benefiting from the integrated structure, the obtained porous oxide could deliver a high specific capacitance of 2.97 F cm^{-2} at 5 mA cm^{-2}. To demonstrate the applicability of our design, we also fabricated both liquid and solid state asymmetric supercapacitors and compared them in this report.

2. EXPERIMENTAL SECTION

2.1. Synthesis of Copper Hydroxide Nanowires. The typical reaction process for the synthesis of CuO nanowires was as follows. First, copper foam (bought from Latech Scientific Supply, Singapore) was cut into small pieces. Then, a piece of copper foam (20 × 20 × 1.5 mm) was cleaned in the ultrasonic bath with absolute ethanol and deionized water to remove adsorbed dust and surface contamination. Then, an aqueous solution was prepared by mixing 20 mL of $(NH_4)S_2O_8$ (0.02 mol L^{-1}) and 20 mL of NaOH (0.5 mol L^{-1}) together. After a few minutes of stirring, the treated copper foam was suspended in the prepared solution. The mixed solution was placed at room temperature for about 30 min (already optimized), and then the copper foam was extracted from the solution, rinsed with water and ethanol several times, and dried at 80 °C in air.

2.2. Synthesis of Nickel Copper Oxide. In a typical synthesis, sodium acetate (2.5 mmol) and nickel sulfate (2.5 mmol) were dissolved in 25 mL of deionized water. After the solution was stirred for 30 min, the above solution was transferred into a Teflon-lined stainless steel autoclave. Hydrothermal synthesis was run under a given temperature of 120 °C for 8 h and then cooled to room temperature. Afterward, the substrates were taken out and cleaned by ultrasonication for several minutes to remove the loosely attached products on the surface, and then dried at 80 °C in an oven overnight.

2.3. Characterizations. The morphology of the prepared samples was examined by using a scanning electron microscope with an X-ray energy dispersive spectrometer (SEM, Zeiss SUPRA40). The crystal structure was identified using X-ray diffraction. Transmission electron microscopy and electron diffraction (TEM, JEOL 2000FX) were employed to obtain high resolution image and structural information. The composition of the products was examined by energy-dispersive X-ray spectroscopy (EDX) attached to the TEM. The surface function groups were investigated by X-ray photoelectron spectroscopy (XPS) (AXIS Ultra). Electrochemical Measurements were carried out in an aqueous KOH (1 M L^{-1}) where NCO/Cu foam was directly used as the working electrode without any polymer binder or conductive addictives, a platinum foil as the counter electrode, and a standard calomel electrode (SCE) as the reference electrode. Electrochemical impedance spectroscopy (EIS) measurements were conducted by applying an AC voltage with 5 mV amplitude in a frequency range of 0.01 Hz to 100 kHz. All of the electrochemical measurements were performed on a Solartron 1470E multichannel potentiostat/cell test system.

2.4. Fabrication of ASCs. The ASCs were assembled by using NCO as positive electrode and reduced graphene oxide as negative electrode. Briefly, the NCO/Cu foam (2 × 1 cm in a rectangular shape) directly acted as the positive electrode without any ancillary materials. The weight gain is around 3 mg. RGO (80%, Graphene Supermarket) and carbon black (20%) were mixed and dispersed in ethanol to obtain a slurry, which was then coated onto the nickel foam current collector (same area as copper foam, 2 × 1 cm) with a spatula. Finally, the as-prepared negative electrode was dried in an oven at 80 °C for 24 h. The mass loading of the material was around 7.5 mg cm^{-2}. KOH/PVA gel was prepared by mixing KOH (6 g) and PVA (6 g) in 60 mL of deionized water and heated at 85 °C under stirring for 10 h. The device to power the LED was the same as the ASC except that the area is 2 × 2 cm instead of 2 × 1 cm. After evaporation of excess water, the two electrodes were assembled together with two pieces of filter paper as a separator (denoted as NCO//RGO ASCs device).

3. RESULTS AND DISCUSSION

This work studies the collector-electrode conversion efficiency by employing a room-temperature solution method together

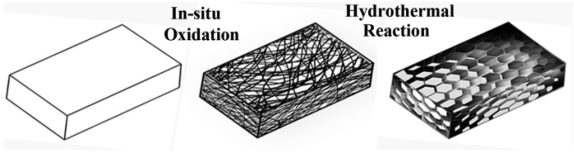

Figure 1. Schematic images showing the two-step collector-electrode conversion: (left) from bulk copper to (middle) copper oxide nanowires through controlled oxidation and then (right) nickel copper oxide electrode through hydrothermal reaction.

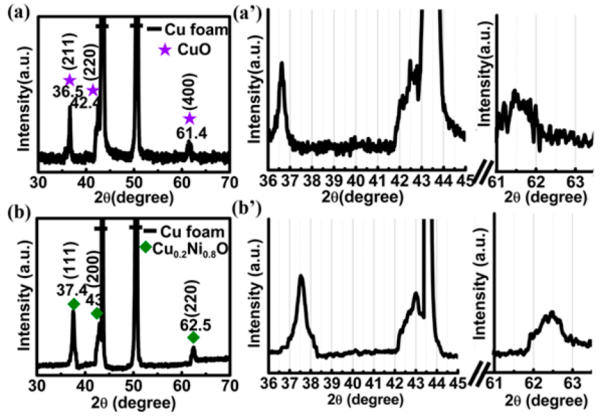

Figure 2. X-ray diffraction patterns of the material prepared in each processing step: (a and a′) after oxidation of copper foam and (b and b′) after hydrothermal reaction.

with the hydrothermal method, characterizing the samples and evaluating the energy storage performances.

Different from many other methods, our approach does not use surfactants (such as CTAB (cetyltrimethylammonium bromide)/SDS (sodium dodecyl sulfonate))[17−19] or hydrolysis agents (such as urea)[20−22] to obtain metal oxides, because it is difficult to remove the surfactant without destroying the structural integrity.[23,24] Furthermore, from an environmental

DOI: 10.1021/acsami.5b02970
ACS Appl. Mater. Interfaces 2015, 7, 15277−15284

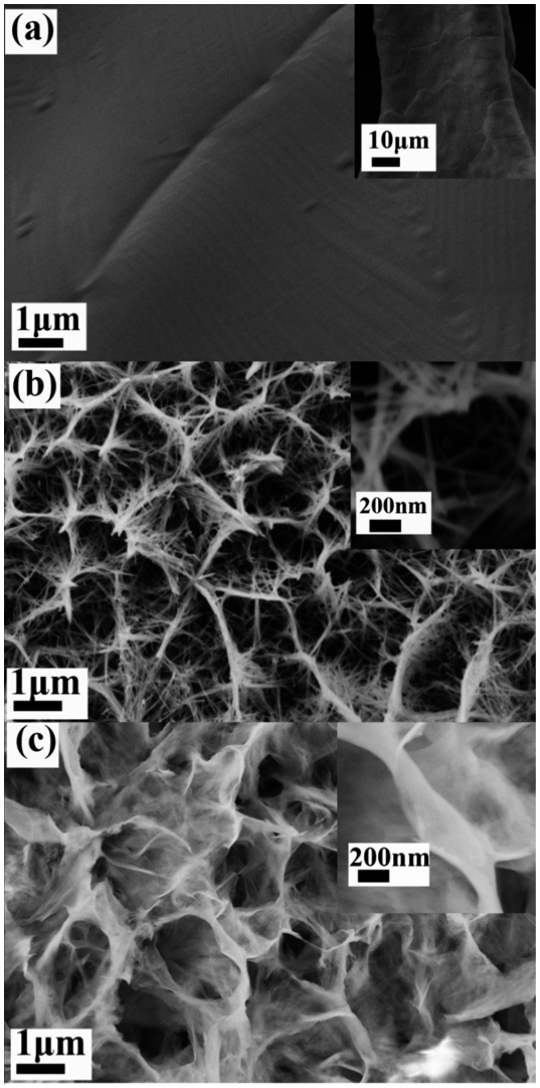

Figure 3. Typical FESEM images of surface morphology of (a) original copper foam; (b) after the first processing step, oxidization; (c) after the second processing step, hydrothermal reaction.

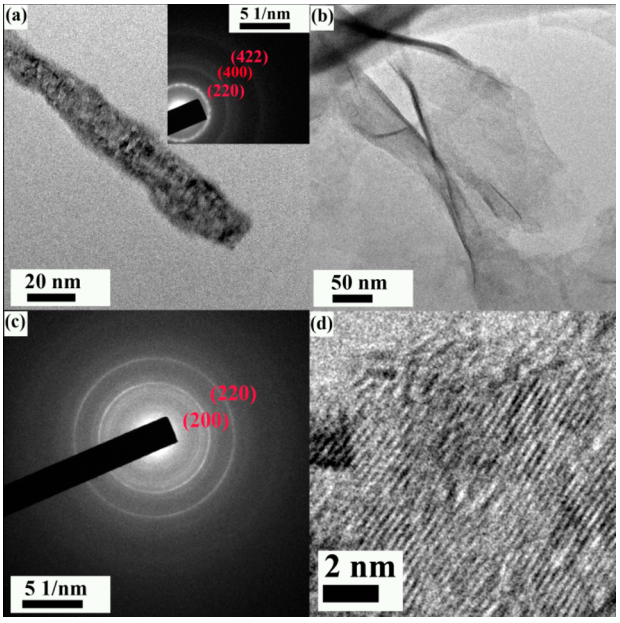

Figure 4. (a) Transmission electron microscopy (TEM) image of a single copper oxide nanowire, and the inset is the SAED pattern; (b) TEM image of hybrid nickel−copper oxide (NCO); (c) SAED pattern of the hybrid nickel−copper oxide; and (d) high-resolution image of the hybrid nickel−copper oxide.

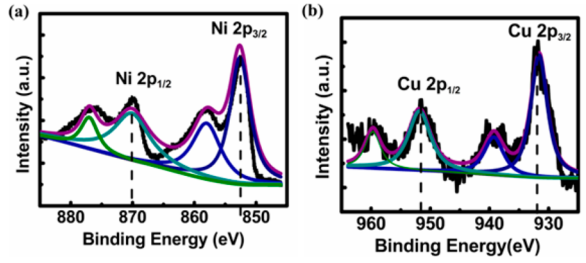

Figure 5. Original and curve-fitting results for the XPS spectrum of NCO: (a) Ni and (b) Cu.

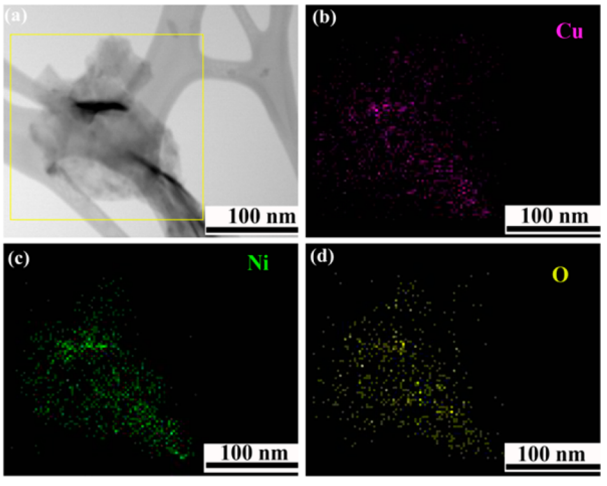

Figure 6. (a) STEM image and the elemental mapping images for (b) Cu, (c) Ni, and (d) O.

perspective, the use of chemicals should be minimized where possible. Besides, the rate of growth of the active material can be controlled more easily when fewer chemicals are consumed. Having good control is necessary to get high-quality material with better stability.[25,26]

3.1. Morphology, Crystal Structure, and Composition.

The synthesis protocol is proposed and illustrated in Figure 1. Nanowires are first formed from the copper substrate via a controlled oxidation process. The nanowires are then transformed into a hybrid in the hydrothermal process. Figure 2a,a′ display the XRD pattern of the copper foam after controlled oxidation. It can be seen that the CuO peaks (JCPDS No.02-1067) are present in addition to Cu. After the hydrothermal process, as seen in Figure 2b,b′, in addition to the strong peaks of copper foam, the XRD pattern can be readily indexed to cubic $Cu_{0.2}Ni_{0.8}O$ phase (JCPDS No.25-1049). However, because of the existence of solid solution $Cu_xNi_{1-x}O$ with similar crystal structure to NiO, there still no plenty of evidence for the proportion of Ni/Cu (4:1).

A 3D network structure of copper foam, possessing flat and clean surfaces without any detectable oxide layer, can be observed in Figure 3a. After the controlled oxidation process, a 3D nanowires network was formed (Figure 3b). These nanowires were confirmed to be CuO based on the XRD

DOI: 10.1021/acsami.5b02970
ACS Appl. Mater. Interfaces 2015, 7, 15277−15284

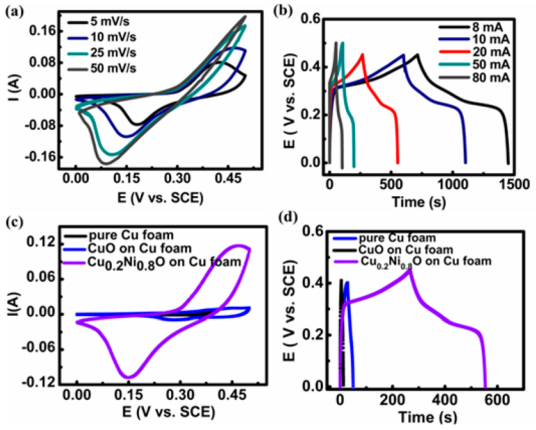

Figure 7. (a) Cyclic voltammetry (CV) curves at different scan rates; (b) galvanostatic charge/discharge (GCD) curves of the hybrid nickel–copper oxide at different current densities; (c) CV curves at 10 mV s^{-1}, and (d) GCD curves at 5 mA cm^{-2} of pure Cu foam, CuO on Cu foam, and $Cu_{0.2}Ni_{0.8}O$ on Cu foam.

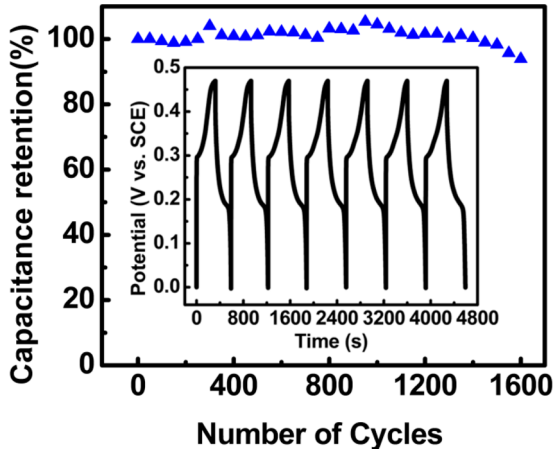

Figure 8. Cycle performance of the hybrid nickel–copper oxide measured at a current density of 5 mA cm^2. The inset is the galvanostatic charge/discharge curves after 1600 cycles.

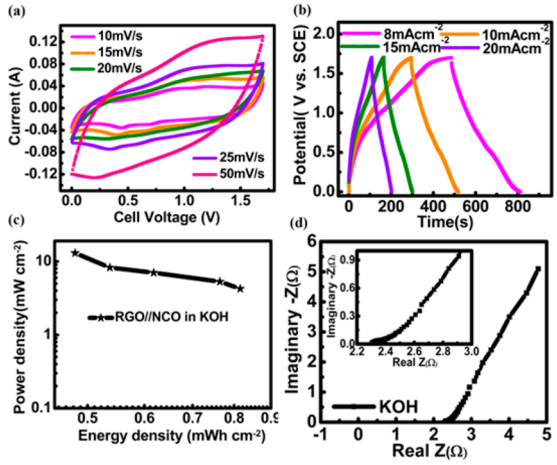

Figure 9. Electrochemical performance of full cell device (a) CV curves of NCO as electrode in 1.7 V SCs using 1 M L^{-1} KOH as electrolyte; (b) galvanostatic charge/discharge curves of the full cell device at different current densities; (c) Ragone plots relate to energy and power densities; and (d) Nyquist plot for the device.

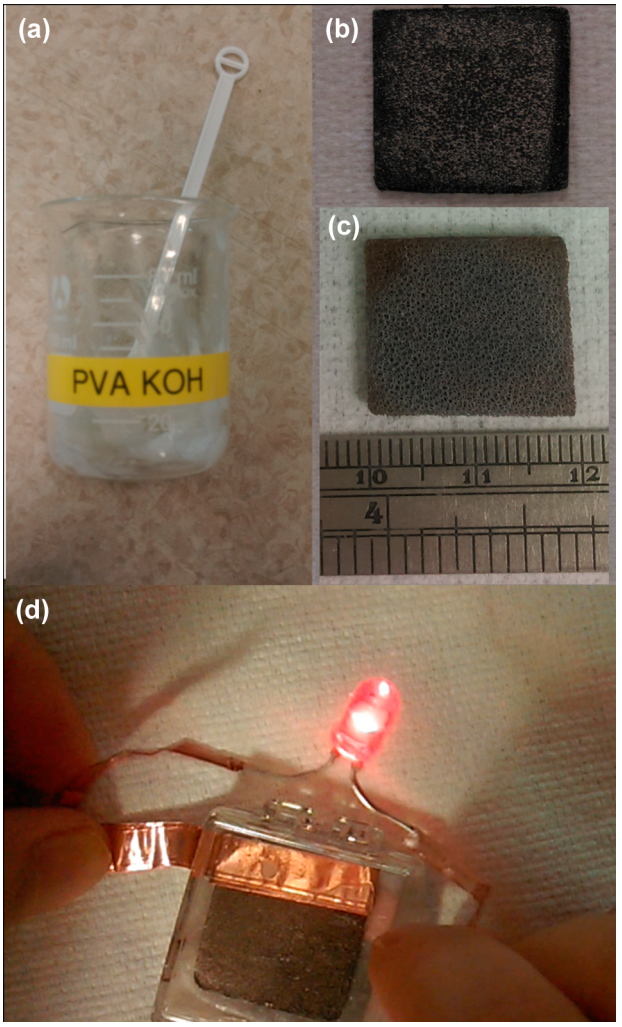

Figure 10. Photos showing the full components: (a) PVA/KOH gel electrolyte, (b) negative electrode on nickel foam and (c) positive electrodes on copper foam; (d) the lighting of an LED, powered by our all-solid supercapacitor full cell that uses PVA-KOH gel electrolyte.

pattern shown in Figure 2b. The nanowires, with a typical length of 2–3 μm and a diameter of 20–50 nm, overlapped with each other, forming interconnected network. After the hydrothermal process in the second step, the nanowires became thicker and nanowalls formed (Figure 3c and inset). The thickness of the wall is about 10–20 nm. The wall branches interconnect with each other, forming a self-supported 3D porous structure. The flakes are connected and form nanosized open channels. The morphology is similar to both the reported graphene pieces[27,28] and the naturally existing honeycomb structure. The folding silk-like morphology (Figure 3b inset) further indicates its ultrathin nature. The honeycomb structure is inspired by the survival of biologic structures after millions of years of natural selection.[29] This structure allows the minimum amount of materials to achieve light weight at low material cost.[30] This morphology is suitable for supercapacitor application because the surface area is high, and the charge generated can easily move from flake to flake.

The TEM image (Figure 4a) shows that the CuO nanowires are thin and rough. The diameter of this nanowire is less than 20 nm. The SAED pattern (Figure 4a inset) reveals that the nanowires are CuO, in agreement with the XRD result. The NCO consists of nanosheets (Figure 4b), consistent with the

DOI: 10.1021/acsami.5b02970
ACS Appl. Mater. Interfaces 2015, 7, 15277–15284

observations from SEM images. The SAED pattern rings (Figure 4b) can be indexed to $Cu_{0.2}Ni_{0.8}O$, consistent with the XRD results. A TEM image of a typical nanosheet edge taken at a higher magnification shows that this ultrathin nanosheet consists of nanograins, and the lattice fringe spacing (Figure 4d) was measured to be 0.24 nm, corresponding to the {111} lattice spacing of $Cu_{0.2}Ni_{0.8}O$.

To further understand the oxidation state of the as-prepared samples, we used X-ray photoelectron spectroscopy (XPS). The surface information on the NCO/Cu could be found from the XPS results displayed in Figure 5. The peak at 852 and 870 eV (Figure 5a) can be interpreted as a nickel(II) state according to literature.[31−33] The binding energy of 933.5 and 951.8 eV (Figure 5b) can be attributed to Cu^{2+} $2p_{3/2}$ and $2p_{1/2}$.[34,35] The presence of Ni^{2+} and Cu^{2+} was ascribed to nickel copper oxide, supporting the phase identification of $Cu_{0.2}Ni_{0.8}O$ from XRD and SAED results. The composition of NCO is further checked by elemental mapping using scanning transmission electron microscopy (STEM). The elemental mapping images (Figure 6) clearly show that Cu, Ni and O coexist in the nanoflakes and are distributed uniformly, which are in good agreement with the XRD and SAED characterizations.

The possible mechanisms for the formation of $Cu_{0.2}Ni_{0.8}O$ are proposed as follows. When a piece of copper is immersed in the solution of sodium hydroxide and ammonium persulfate, $Cu(OH)_2$, derived from the simple liquid−solid reaction eq 1, can nucleate and grow into nanowires on the copper substrate.

$$Cu + 4NaOH + (NH_4)_2S_2O_8 \rightarrow Cu(OH)_2 + 2Na_2SO_4 + 2NH_3 + 2H_2O \quad (1)$$

After drying in an oven, the copper hydroxide is transformed into copper oxide, and the reaction is shown in eq 2.

$$Cu(OH)_2 \rightarrow CuO + H_2O \quad (2)$$

The exact mechanism for the formation of nanowires is still unclear according to literature.[36,37] We propose the following explanation: in a complex and nonequilibrium reaction system, the highly alkaline conditions favor the coordination of OH^- group to Cu^{2+} chains along one direction. Juxtaposing the chains and the difference in the growth rate of different crystal faces finally determine the nanowire morphology.[38−40]

To control the size and porosity of copper nanowires, we altered the experimental parameter. When the time is short, the nanowires are scattered and short, but when the time is too long, agglomeration and other flakes could be seen. Thus, we choose the optimized time (30 min) to grow the nanowires.

In the second processing step, the sample obtained from the first step is immersed in a solution of nickel sulfate and sodium acetate. Hydrothermal processing is then performed. Because nickel and copper have similar radii and their oxides have similar crystal structure, they are able to precipitate together and $Cu_{0.2}Ni_{0.8}O$ is formed eq 3.

$$CuO + 4NiSO_4 + 8NaCH_3COO + 4H_2O \rightarrow 5Cu_{0.2}Ni_{0.8}O + 4Na_2SO_4 + 8CH_3COOH \quad (3)$$

As the second step (hydrothermal) is performed under high temperature and high pressure hydrothermal conditions, the reaction is promoted. The detailed mechanism is still under investigation.

3.2. Electrochemical Performance of $Cu_{0.2}Ni_{0.8}O$ in Three-Electrode Configuration. To evaluate the electrochemical performance, cyclic voltammetry (CV) and galvanic charge−discharge (GCD) measurements were performed. The shape of the CV curves shown in Figure 7a indicates pseudocapacitive behavior. The electrochemical electron-transfer process mainly involves the Faradaic redox process related to Ni^{2+}/Ni^{3+}.[41] The much reduced peak separation (only 0.16 V) of our $Cu_{0.2}Ni_{0.8}O$ sample demonstrates greatly enhanced reaction kinetics. This result shows high rate capability which is important in supercapacitor application. It is also noted that the shapes of CV curves do not vary much with the increase of scan rates (from 5 to 50 mV s^{-1}). Only a slightly shifted peak position is observed, suggesting fast electron transport due to an excellent contact between $Cu_{0.2}Ni_{0.8}O$ and the Cu current collector. Galvanic charge−discharge results are presented in Figure 7b, indicating a rapid response. The electrochemical performance of pure CuO nanowires synthesized from the first step is revealed in Figure S2 (SI). We note that because the current collector is consumed, the use of areal capacitance is more reasonable. The comparison of pure Cu foam current collector, CuO on Cu foam (product of the first step), and $Cu_{0.2}Ni_{0.8}O$ on Cu foam (product of the second step) is shown in Figure 7c,d. From the result, pure Cu foam has a very small capacitance about 0.005 F cm^{-2}. It can also be seen that the CuO itself does contribute to the supercapacitor performance. Because the weight decreases after the first step, the calculated areal capacitance of copper oxide nanowires is about 0.08 F cm^{-2}. While an areal capacitance of 3 F cm^{-2} is obtained for $Cu_{0.2}Ni_{0.8}O$. The above result also shows that the contribution of pure copper nanowires is very small (less than 3%) and the improvement after the hydrothermal step is significant (almost 40 times). The gravimetric capacitance results are estimated to be about 2300−2450 F g^{-1}. (Note that the weight here is the weight gain before and after the growth. Though the Cu foam is consumed, the total weight is increased by 5 mg after the completion of both processes.)

It is known that that the specific capacitance value depends on the constant current density. A higher current density gives a lower specific capacitance because of ion diffusion and internal resistance. To show that our devices are primary energy storage devices with high rate capability, capacitances at high current densities are also measured. It is worth mentioning that the capacitance values do not decrease much from 1 mA (Supporting Information, Figure S1) to 80 mA (Figure 7b), indicating the good rate performance of the electrode. The capacitance achieved at 20 mA is 2309 F g^{-1}, similar to the capacitance obtained at a low current of 1 mA. The counterions hereby can reach or leave the surface of the $Cu_{0.2}Ni_{0.8}O$ electrode quickly even at a high charge−discharge rate. In addition, $Cu_{0.2}Ni_{0.8}O$ with thin layers can shorten the charge transport distance. Therefore, the porous honeycomb-like structures of $Cu_{0.2}Ni_{0.8}O$ enable high dynamics of charge propagation and short electron transport paths and consequently improve the electrochemical performance, supporting literature expectations.[42,43]

Cycle life of a supercapacitor is a crucial parameter for its practical application. Galvanic charge/discharge measurement at 5 mA cm^{-2} is performed (Figure 8). Excellent specific capacitance retention is found, with only 6.5% decay after 1600 cycles. It is also observed that the structure/morphology remained almost intact after 1600 cycles (Figure S5a, SI, SEM image of the material after cycling). The good mechanical contact between the active material and the current collector derived from the direct oxidation of current collector is favorable for long cycles. There are three possible reasons for the remarkable electrochemical stability: (1) almost complete and

DOI: 10.1021/acsami.5b02970
ACS Appl. Mater. Interfaces 2015, 7, 15277−15284

uniform coverage of $Cu_{0.2}Ni_{0.8}O$ on the copper foam which can provide equally efficient pathway for electronic and ionic transport, (2) good contact between the active $Cu_{0.2}Ni_{0.8}O$ electrode and the Cu current collector because the current collector itself participated in the formation of the active material, and (3) the unique morphology of the honeycomb-like $Cu_{0.2}Ni_{0.8}O$ is stable. We used ultrasonication to test the quality of the contact. After ultrasonication for half an hour, no visible particles could be seen in the beaker, and the weight change is less than 0.1%.

3.3. Full Cell of $Cu_{0.2}Ni_{0.8}O$ Based Asymmetric Supercapacitors (ASCs). To further assess the NCO electrode for commercial application, we have fabricated and tested ASCs in both liquid and solid electrolyte.

Asymmetric supercapacitors consisting of anode, cathode, and electrolyte were made in this work (Experimental Section). The advantage of a asymmetric full cell is the combination of a battery-like Faradaic electrode as the energy source and a capacitive electrode as the power source, offering the advantages of both supercapacitors (rate, cycle life) and advanced batteries (energy density).[44,45] The attractive features lie in the high specific capacitance and the wider operating potential window. The weight ratio of RGO to NCO was controlled at about 5:1. This ratio was based on both experimental optimization and two theories. According to Zheng's work, the energy density could reach the maximum value when the ratio of negative electrode to positive electrode was 4:1.[46] According to the theory of balancing the charge stored at negative electrode and positive electrode[47] and by calculating the window and capacitance of the two electrodes, the mass should be 6:1. Thus, we chose the optimal one to be 5:1.

The capacitive behavior of the full cell is investigated in this work. To avoid possible atypical data, the new full cell was polarized for a few cycles until stabilization[48] and the stable electrochemical window was determined before cycling the full cell. After tentative examinations, the stable potential window of the ASC can be determined to be 1.7 V without obvious polarization curves or observable oxygen evolution. It is found that the voltammograms remain the same without any obvious distortion even when the scan rate increases to 50 mV s^{-1}. This suggests a desirable high-rate power delivery. The calculated specific capacitance of the asymmetric full cell is 2.03 F cm^{-2} (specific capacitance of the entire cell was calculated to be about 148 F g^{-1}) at a current density of 5 mA cm^{-2}. The specific capacitance, energy density and power density of a supercapacitor is calculated from the galvanostatic discharge process according to eqs 4, 5, and 6 following literature.[49,50]

$$C_{sp} = \frac{I\Delta t}{S\Delta V} \tag{4}$$

$$E = \frac{1}{2}CV^2 \tag{5}$$

where, I is the discharge current (A), Δt is the discharge time (s), ΔV is the voltage change (V), and S is the area of the electrode (the area of copper current collector, cm^2). Figure 9a,b show CV curves at different scanning rates and galvanostatic charge/discharge curves at different current densities for the full cell. It can be seen that the CV curves are roughly rectangular, and the discharge curves are almost linear. Figure 9c shows Ragone plots, in which the superior device performance of our asymmetric supercapacitor is highlighted. The gravimetric energy density (based on the weight gain of the active material in both electrodes, here 3 + 15 = 18 mg) decreases only from 90 to 53 Wh kg^{-1} when the power density greatly increases from 472 up to 1445 W kg^{-1}. Because the weight of the active material cannot be estimated accurately, we also report the areal energy density and power density in addition to the gravimetrical ones. The areal energy densities (here, based on area of copper current collector, is 2 cm^2) of the full cell calculated is from 0.5 to 0.8 mWh cm^{-2} at the different power densities from 4.2 to 13 mW cm^{-2}. The match of energy density and power density of the full cell uncovers the promising application of supercapacitors achieved by using this novel approach in converting electrode from part of substrate (current connector).

Because the use of solid state electrolytes offers a number of desirable advantages such as ease of handling/packaging, scalability, less leakage, improved safety and flexibility, high reliability, wide operation temperature range, and so forth,[51−54] we have also assembled a solid state supercapacitor full cell using gel electrolyte and studied its electrochemical performance.

From the CV curves in the three-electrode configuration (Supporting Information, Figure S2a), the redox reaction in the gel electrolyte is less pronounced and the peak current is lower than that of the liquid electrolyte. The most recognizable difference from the shape of CV curves is the disappearance of the anodic peak. It has been reported that the insertion of bulky ions may shift the peak positions.[55,56] In our case, the redox peak shifted positively, overlapping the peak of oxygen evolution. This could because that inserting/expulsing bulky PVA chains in the solid electrolyte needs a higher overpotential than that of small ions in water. It is reasonable or understandable that the electrode in gel electrolyte cannot perform as well as in a liquid electrolyte, as it is difficult to retain a close solid−solid electrode−electrolyte interface.[57]

To scrutinize the charge transfer, electrochemical kinetics, and internal resistance differences between the liquid and solid electrolyte, factors which influence the supercapacitor performance, electrochemical impedance spectroscopy (EIS) measurements are performed in the same setup as the CV and GCD studies. Figure 9d and Figure S4d (SI) show the Nyquist plots when employing KOH and KOH/PVA gel polymer for the ASCs with enlarged high frequency regions (inset). Both have ideal electrochemical capacitance behavior, for example, imaginary parts of impedance at the low-frequency region are nearly linear, and a slightly depressed semicircle at higher frequency.[58,59] In the high-frequency region, the intersection of the curve at real part axis indicates the bulk resistance of the electrochemical system (electrolyte resistance, intrinsic resistance of substrate, and contact resistance at the active material/current collector interface).[60] The diameter of semicircle is determined by the charge transfer resistance (R_{ct}) at the interface between the electrode material and the electrolyte.[61] From the enlarged view of the higher frequency semicircles, it can be seen that the supercapacitor with gel electrolyte has a slightly lower inner resistance but a larger charge transfer resistance. Better accessibility of the pores to the electrolyte ions of the liquid electrolyte than those of the gel electrolyte, which is confirmed by the reduction of the semicircle width, is shown.

To evaluate the feasibility of our supercapacitor device, we used it to power small electronic devices. The device was fabricated by sandwiching a KOH/PVA gel between a positive electrode (our NCO/Cu foam) and a negative electrode (RGO/Ni foam). Two pieces of filter paper were also used as the separator to avoid short circuit. Each component of the supercapacitor device is shown in Figure 10. It should be

DOI: 10.1021/acsami.5b02970
ACS Appl. Mater. Interfaces 2015, 7, 15277−15284

highlighted that this is a fully solid state supercapacitor without sealing and does not have the risk of liquid leaking. After charging for only 30 s to ~1.75 V, the device was able to light up a 5 mm diameter red light emitting diode (1.8 V, RS component) for 2 min.

4. CONCLUSIONS

A nickel copper oxide electrode is converted from part of a copper collector (substrate) by two-step chemical processing without any surfactant or precipitate controlling agents. The advantage of this novel process is that the copper foam current collector itself participates in the formation of the active material so that the contact problem between active material and current collector does not exist anymore. A unique honeycomb-like morphology is formed on the electrode and was found to be stable. The application of this electrode/collector in supercapacitor is very promising. A high areal capacitance of 2.97 F cm^{-2} at a current density of 5 mA cm^{-2} is achieved. An asymmetric full cell prototype has been assembled, using our material as the anode and reduced graphene oxides as the cathode. The ASC full cell is capable of affording a high areal capacitance of 2.03 F cm^{-2} and energy density of 0.8 mWh cm^{-2} at room temperature in liquid electrolyte. A solid-state supercapacitor full cell incorporating our material is assembled and shown to be able to light up a LED for minutes.

■ ASSOCIATED CONTENT

Supporting Information

GCD curves of NCO at small current, CV and GCD curves pure CuO/Cu foam, CV and GCD cures of NCO in gel electrolyte, asymmetric supercapacitor of NCO in gel electrolyte, SEM images of NCO after cycling in liquid and gel electrolyte, respectively. The Supporting Information is available free of charge on the ACS Publications website at DOI: 10.1021/acsami.5b02970.

■ AUTHOR INFORMATION

Corresponding Author

* Tel.:+65-65164632. E-mail: msegongh@nus.edu.sg.

Notes

The authors declare no competing financial interest.

■ ACKNOWLEDGMENTS

The support of Singapore MOE Tier 2 grant R-284-000-125-112 is appreciated.

■ REFERENCES

(1) Wang, G.; Wang, H.; Lu, X.; Ling, Y.; Yu, M.; Zhai, T.; Tong, Y.; Li, Y. Solid-State Supercapacitor Based on Activated Carbon Cloths Exhibits Excellent Rate Capability. *Adv. Mater.* **2014**, *26*, 2676−2682.

(2) Xia, X.; Chao, D.; Fan, Z.; Guan, C.; Cao, X.; Zhang, H.; Fan, H. J. A New Type of Porous Graphite Foams and Their Integrated Composites with Oxide/Polymer Core/Shell Nanowires for Supercapacitors: Structural Design, Fabrication, and Full Supercapacitor Demonstrations. *Nano Lett.* **2014**, *14* (3), 1651−1658.

(3) Giri, S.; Ghosh, D.; Das, C. K. Growth of Vertically Aligned Tunable Polyaniline on Graphene/ZrO_2 Nanocomposites for Supercapacitor Energy-Storage Application. *Adv. Funct. Mater.* **2014**, *24*, 1312−1324.

(4) Rakhi, B.; Chen, W.; Hedhili, M. N.; Cha, D.; Alshareef, H. N. Enhanced Rate Performance of Mesoporous Co_3O_4 Nanosheet Supercapacitor Electrodes by Hydrous RuO_2 Nanoparticle Decoration. *ACS Appl. Mater. Interfaces* **2014**, *6* (6), 4196−4206.

(5) Wang, W.; Guo, S.; Bozhilov, K. N.; Yan, D.; Ozkan, M.; Ozkan, C. S. Intertwined Nanocarbon and Manganese Oxide Hybrid Foam for High-Energy Supercapacitors. *Small* **2013**, *9* (21), 3714−3721.

(6) Huang, L.; Chen, D.; Ding, Y.; Feng, S.; Wang, Z. L.; Liu, M. Nickel−Cobalt Hydroxide Nanosheets Coated on $NiCo_2O_4$ Nanowires Grown on Carbon Fiber Paper for High-Performance Pseudocapacitors. *Nano Lett.* **2013**, *13*, 3135−3139.

(7) Li, J.; Yang, M.; Wei, J.; Zhou, Z. Preparation and Electrochemical Performances of Doughnut-Like $Ni(OH)_2$ $Co(OH)_2$ Composites as Pseudocapacitor Materials. *Nanoscale* **2012**, *4*, 4498−4503.

(8) Wang, H. L.; Gao, Q. M.; Jiang, L. Facile Approach to Prepare Nickel Cobaltite Nanowire Materials for Supercapacitors. *Small* **2011**, *7*, 2454−2459.

(9) Wang, Y. G.; Xia, Y. Y. Electrochemical Capacitance Characterization of NiO with Ordered Mesoporous Structure Synthesized by Template SBA-15. *Electrochim. Acta* **2006**, *51*, 3223−3227.

(10) Lee, J. W.; Ko, J. M.; Kim, J.-D. Hierarchical Microspheres Based on α-$Ni(OH)_2$ Nanosheets Intercalated with Different Anions: Synthesis, Anion Exchange, and Effect of Intercalated Anions on Electrochemical Capacitance. *J. Phys. Chem. C* **2011**, *115*, 19445−19454.

(11) Xing, W.; Li, F.; Yan, Z. F.; Lu, G. Q. Synthesis and Electrochemical Properties of Mesoporous Nickel Oxide. *J. Power Sources* **2004**, *134*, 324−330.

(12) Yang, G. W.; Xu, C. L.; Li, H. L. Electrodeposited Nickel Hydroxide on Nickel Foam with Ultrahigh Capacitance. *Chem. Commun.* **2008**, 6537−6539.

(13) Yuan, Y. F.; Xia, X. H.; Wu, J. B.; Yang, J. L.; Chen, Y. B.; Guo, S. Y. Nickel Foam-Supported Porous $Ni(OH)_2$/NiOOH Composite Film as Advanced Pseudocapacitor Material. *Electrochim. Acta* **2011**, *56*, 2627−2632.

(14) Simon, P.; Gogotsi, Y. Materials for Electrochemical Capacitors. *Nat. Mater.* **2008**, *7*, 845−854.

(15) Lokhande, C. D.; Dubal, D. P.; Joo, O. S. Metal Oxide Thin Film Based Supercapacitors. *Curr. Appl. Phys.* **2011**, *11*, 255−270.

(16) Dong, W.; Rolison, D. R.; Dunn, B. Electrochemical Properties of High Surface Area Vanadium Oxide Aerogels. *Electrochem. Solid-State Lett.* **2000**, *3*, 457−489.

(17) Berry, V.; Gole, A.; Kundu, S.; Murphy, C. J.; Saraf, R. F. Deposition of CTAB-Terminated Nanorods on Bacteria to Form Highly Conducting Hybrid Systems. *J. Am. Chem. Soc.* **2005**, *127*, 17600−17601.

(18) Maurer-Jones, M. A.; Lin, Y.-S.; Haynes, C. L. Functional Assessment of Metal Oxide Nanoparticle Toxicity in Immune Cells. *ACS Nano* **2010**, *4*, 3363−3373.

(19) Chen, P.-C.; Shen, G.; Shi, Y.; Chen, H.; Zhou, C. Preparation and Characterization of Flexible Asymmetric Supercapacitors Based on Transition-Metal-Oxide Nanowire/Single-Walled Carbon Nanotube Hybrid Thin-Film Electrodes. *ACS Nano* **2010**, *4* (8), 4403−4411.

(20) Gao, Y.; Zhang, Z.; Wu, J.; Yi, X.; Zheng, A.; Umar, A.; O'Haree, D.; Wang, Q. Comprehensive Investigation of CO_2 Adsorption on Mg−Al−CO_3 LDH-Derived Mixed Metal Oxides. *J. Mater. Chem. A* **2013**, *1*, 12782−12790.

(21) Fang, Q.; Xuan, S.; Jiang, W.; Gong, X. Yolk-like Micro/Nanoparticles with Superparamagnetic Iron Oxide Cores and Hierarchical Nickel Silicate Shells. *Adv. Funct. Mater.* **2011**, *21*, 1902−1909.

(22) Xiong, S.; Chen, J. S.; Lou, X. W.; Zeng, H. C. Mesoporous Co_3O_4 and CoO@C Topotactically Transformed from Chrysanthemum-like $Co(CO_3)_{0.5}(OH)\cdot 0.11H_2O$ and Their Lithium-Storage Properties. *Adv. Funct. Mater.* **2012**, *22*, 861−871.

(23) Ulagappan, N.; Rao, C. N. R. Mesoporous Phases Based on SnO_2 and TiO_2. *Chem. Commun.* **1996**, 1685−1686.

(24) Sudhakar Reddy, J.; Sayari, A. Nanoporous Zirconium Oxide Prepared Using the Supramolecular Templating Approach. *Catal. Lett.* **1996**, *38*, 219−223.

(25) Kondo, J. N.; Takahara, Y.; Lu, D.; Domen, K. Mesoporous Ta Oxide. 2. Improvement of the Synthetic Method and Observation of Mesostructure Formation. *Chem. Mater.* **2001**, *13* (4), 1200−1206.

DOI: 10.1021/acsami.5b02970
ACS Appl. Mater. Interfaces 2015, 7, 15277−15284

(26) Parvulescu, V. I.; Bonnemann, H.; Enduschat, U.; Rufinska, A.; Lehmann, Ch. W.; Tesche, B.; Poncelet, G. Preparation and Characterisation of Mesoporous Zirconium Oxide. *Appl. Catal., A* **2001**, *214*, 273−287.
(27) Zhang, L.; Shi, G. Preparation of Highly Conductive Graphene Hydrogels for Fabricating Supercapacitors with High Rate Capability. *J. Phys. Chem. C* **2011**, *115* (34), 17206−17212.
(28) Huang, G.; Chen, T.; Chen, W.; Wang, Z.; Chang, K.; Ma, L.; Huang, F.; Chen, D.; Lee, J. Y. Graphene-Like MoS_2/Graphene Composites: Cationic Surfactant-Assisted Hydrothermal Synthesis and Electrochemical Reversible Storage of Lithium. *Small* **2013**, *9*, 3693−3703.
(29) Bar-Cohen, Y. Biomimetics—Using Nature to Inspire Human Innovation. *Bioinspiration Biomimetics* **2006**, *1*, 1−12.
(30) Yu, X.; Lu, B.; Xu, Z. Super Long-Life Supercapacitors Based on the Construction of Nanohoneycomb-Like Strongly Coupled $CoMoO_4$−3D Graphene Hybrid Electrodes. *Adv. Mater.* **2014**, *26*, 1044−1051.
(31) Siriwardane, R.; Poston, J. Chemical-Looping Combustion of Simulated Synthesis Gas Using Nickel Oxide Oxygen Carrier Supported on Bentonite. *Energy Fuels* **2007**, *21*, 1582−1591.
(32) Fominykh, K.; Feckl, J. M.; Sicklinger, J.; Döblinger, M.; Böcklein, S.; Ziegler, J.; Peter, L.; Rathousky, J.; Scheidt, E. W.; Bein, T.; Rohlfing, D. F. Ultrasmall Dispersible Crystalline Nickel Oxide Nanoparticles as High-Performance Catalysts for Electrochemical Water Splitting. *Adv. Funct. Mater.* **2014**, *24*, 3123−3129.
(33) Chusuei, C. C.; Brookshier, M. A.; Goodman, D. W. Correlation of Relative X-ray Photoelectron Spectroscopy Shake-up Intensity with CuO Particle Size. *Langmuir* **1999**, *15*, 2806−2808.
(34) La Rosa-Toro, A.; Berenguer, R.; Quijada, C.; Montilla, F.; Morallón, E.; Vázquez, J. L. Preparation and Characterization of Copper-Doped Cobalt Oxide Electrodes. *J. Phys. Chem. B* **2006**, *110*, 24021−24029.
(35) Wu, C. K.; Yin, M.; O'Brien, S.; Koberstein, J. T. Quantitative Analysis of Copper Oxide Nanoparticle Composition and Structure by X-ray Photoelectron Spectroscopy. *Chem. Mater.* **2006**, *18*, 6054−6058.
(36) Zhang, W.; Wen, X.; Yang, S.; Berta, Y.; Wang, Z. L. Single-Crystalline Scroll-Type Nanotube Arrays of Copper Hydroxide Synthesized at Room Temperature. *Adv. Mater.* **2003**, *15*, 822−825.
(37) Zhang, W.; Wen, X.; Yang, S. Controlled Reactions on a Copper Surface: Synthesis and Characterization of Nanostructured Copper Compound Films. *Inorg. Chem.* **2003**, *42*, 5005−5014.
(38) Wen, X.; Zhang, W.; Yang, S.; Dai, Z. R.; Wang, Z. L. Solution Phase Synthesis of $Cu(OH)_2$ Nanoribbons by Coordination Self-Assembly Using Cu_2S Nanowires as Precursors. *Nano Lett.* **2002**, *2* (12), 1397−1401.
(39) Hou, H.; Xie, Y.; Li, Q. Large-Scale Synthesis of Single-Crystalline Quasi-Aligned Submicrometer CuO Ribbons. *Cryst. Growth Des.* **2005**, *5*, 201−205.
(40) Yang, D.; Liu, P.; Gao, Y.; Wu, H.; Cao, Y.; Xiao, Q.; Li, H. Synthesis, Characterization, and Electrochemical Performances of Core-Shell $Ni(SO_4)_{0.3}(OH)_{1.4}$/C and NiO/C Nanobelts. *J. Mater. Chem.* **2012**, *22*, 7224−7231.
(41) Wang, H.; Casalongue, H. S.; Liang, Y.; Dai, H. Ni(OH)2 Nanoplates Grown on Graphene as Advanced Electrochemical Pseudocapacitor Materials. *J. Am. Chem. Soc.* **2010**, *132* (21), 7472−7477.
(42) Wang, X.; Wang, X.; Huang, W.; Sebastian, P. J.; Gamboa, S. Sol−Gel Template Synthesis of Highly Ordered MnO_2 Nanowire Arrays. *J. Power Sources* **2005**, *140*, 211−215.
(43) Xu, C.; Zhao, Y.; Yang, G.; Li, F.; Li, H. Mesoporous Nanowire Array Architecture of Manganese Dioxide for Electrochemical Capacitor Applications. *Chem. Commun.* **2009**, 7575−7577.
(44) Wu, Z. S.; Ren, W.; Wang, D. W.; Li, F.; Liu, B.; Cheng, H. M. High-Energy MnO_2 Nanowire/Graphene and Graphene Asymmetric Electrochemical Capacitors. *ACS Nano* **2010**, *4* (10), 5835−5842.
(45) Zhao, X.; Sánchez, B. M.; Dobsona, P. J.; Grant, P. S. The Role of Nanomaterials in Redox-Based Supercapacitors for Next Generation Energy Storage Devices. *Nanoscale* **2011**, *3*, 839−855.
(46) Zheng, J. P. The Limitations of Energy Density of Battery/Double-Layer Capacitor Asymmetric Cells. *J. Electrochem. Soc.* **2003**, *150*, A484−A491.
(47) Chen, P.-C.; Shen, G.; Shi, Y.; Chen, H.; Zhou, C. Preparation and Characterization of Flexible Asymmetric Supercapacitors Based on Transition-Metal-Oxide Nanowire/Single-Walled Carbon Nanotube Hybrid Thin-Film Electrodes. *ACS Nano* **2010**, *4*, 4403−4411.
(48) Lang, J. W.; Kong, L. B.; Liu, M.; Luo, Y. C.; Kang, L. Asymmetric Supercapacitors Based on Stabilized α-Ni(OH)2 and Activated Carbon. *J. Solid State Electrochem.* **2010**, *14*, 1533−1539.
(49) Zhang, L. L.; Zhao, X. S. Carbon-Based Materials as Supercapacitor Electrodes. *Chem. Soc. Rev.* **2009**, *38*, 2520−2531.
(50) Stoller, M. D.; Ruoff, R. S. Best Practice Methods for Determining an Electrode Material's Performance for Ultracapacitors. *Energy Environ. Sci.* **2010**, *3*, 1294−1301.
(51) Yang, P.; Ding, Y.; Lin, Z.; Chen, Z.; Li, Y.; Qiang, P.; Ebrahimi, M.; Mai, W.; Wong, C. P.; Wang, Z. L. Low-Cost High-Performance Solid-State Asymmetric Supercapacitors Based on MnO_2 Nanowires and Fe_2O_3 Nanotubes. *Nano Lett.* **2014**, *14* (2), 731−736.
(52) El-Kady, M. F.; Strong, V.; Dubin, S.; Kaner, R. B. Laser Scribing of High-Performance and Flexible Graphene-Based Electrochemical Capacitors. *Science* **2012**, *335*, 1326−1330.
(53) Lu, X.; Zhai, T.; Zhang, X.; Shen, Y.; Yuan, L.; Hu, B.; Gong, L.; Chen, J.; Gao, Y.; Zhou, J.; Tong, Y.; Wang, Z. L. WO_{3x}@Au@MnO_2 Core−Shell Nanowires on Carbon Fabric for High-Performance Flexible Supercapacitors. *Adv. Mater.* **2012**, *24*, 938−944.
(54) Randriamahazaka, H.; Plesse, C.; Teyssie, D.; Chevrot, C. Relaxation Kinetics of Poly(3,4-ethylenedioxythiophene) in 1-Ethyl-3-Methylimidazolium Bis((trifluoromethyl)sulfonyl)Amide Ionic Liquid During Potential Step Experiments. *Electrochim. Acta* **2005**, *50*, 1515−1522.
(55) Pringle, J. M.; Ngamna, O.; Lynam, C.; Wallace, G. G.; Forsyth, M.; MacFarlane, D. R. Conducting Polymers with Fibrillar Morphology Synthesized in a Biphasic Ionic Liquid/Water System. *Macromolecules* **2007**, *40*, 2702−2711.
(56) Schneider, O.; Bund, A.; Ispas, A.; Borissenko, N.; El Abedin, S. Z.; Endres, F. An EQCM Study of the Electropolymerization of Benzene in an Ionic Liquid and Ion Exchange Characteristics of the Resulting Polymer Film. *J. Phys. Chem. B* **2005**, *109*, 7159−7168.
(57) Goodenough, J. B. Evolution of Strategies for Modern Rechargeable Batteries. *Acc. Chem. Res.* **2013**, *46*, 1053−1061.
(58) Taberna, P. L.; Simon, P.; Fauvarque, J. F. Electrochemical Characteristics and Impedance Spectroscopy Studies of Carbon-Carbon Supercapacitors. *J. Electrochem. Soc.* **2003**, *150*, A292−A300.
(59) Wang, J.; Xu, Y.; Yan, F.; Zhu, J.; Wang, J. Template-Free Prepared Micro/Nanostructured Polypyrrole with Ultrafast Charging/Discharging Rate and Long Cycle Life. *J. Power Sources* **2011**, *196*, 2373−2379.
(60) Wu, M. S.; Wang, M. J.; Jow, J. J. Fabrication of Porous Nickel Oxide Film with Open Macropores by Electrophoresis and Electrodeposition for Electrochemical Capacitors. *J. Power Sources* **2010**, *195*, 3950−3955.
(61) Wang, K. P.; Teng, H. Structural Feature and Double-Layer Capacitive Performance of Porous Carbon Powder Derived from Polyacrylonitrile-Based Carbon Fiber. *J. Electrochem. Soc.* **2007**, *154*, A993−A998.

DOI: 10.1021/acsami.5b02970
ACS Appl. Mater. Interfaces 2015, 7, 15277−15284